Supplementary Information (SI) for Energy & Environmental Science.

Supplementary Information

Integrated one-step dry process enabling prelithiated thick electrodes without primer coating for high energy density and initial Coulombic efficiency

Hyun-Wook Lee,[†a] Woojin Jeong,[†b,c] Seongsoo Park,[†d] Ho-Jeong Ji,[a] Ji-Su Woo,[a] Juhyun Lee,[b,e] Ye-Jin An,[a] Yu-Chan Hwang,[a] Dong-Ha Kim,[a] Hongjun Chang,[d] Minseok Kim,[b] Mikang Jeong,[b] Moonsu Yoon,[b] Dongsoo Lee,[b] Jongsoon Kim,[f,g] Zheng-Long Xu,[h] Taeseup Song,[c,i] Janghyuk Moon,[*d] Junghyun Choi,[*b] Won-Jin Kwak[*a]

[a]School of Energy and Chemical Engineering, UNIST, Ulsan, 44919, Republic of Korea
E-mail: wjkwak@unist.ac.kr

[b]School of Chemical, Biological and Battery Engineering, Gachon University, Seongnam, 13120, Repubilc of Korea
E-mail: junghchoi@gachon.ac.kr

[c]Department of Energy Engineering, Hanyang University, Seoul, 04763, Republic of Korea

[d]Department of Energy Systems Engineering, Chung-Ang University, Seoul, 06974, Republic of Korea
E-mail: jhmoon84@cau.ac.kr

[e]Department of Materials Science and Engineering, Pusan National University, Busan, 46241, Republic of Korea

[f]Department of Energy Science, Sungkyunkwan University (SKKU), Suwon 16419, Republic of Korea

[g]SKKU Institute of Energy Science and Technology (SIEST), Sungkyunkwan University, Suwon, 16419, Republic of Korea

[h]Department of Industrial and Systems Engineering, The Hong Kong Polytechnic University, Hung Hom, Hong Kong SAR, China

[i]Department of Battery Engineering, Hanyang University, Seoul, 04763, Republic of Korea

E-mail: jhmoon84@cau.ac.kr (J.M.); junghchoi@gachon.ac.kr (J.C.); wjkwak@unist.ac.kr (W.-J.K.)

[†]H.-W. L., W. J. and S. P. contributed equally to this work.

Experimental section

Preparation of dry Si/G electrode

The dry-processed anode was fabricated by blending a silicon–carbon (Si/C, Hansol Chemical) composite with artificial graphite (G49, Shanshan) in a 9:91 weight ratio. Carbon black (Super-P, Imerys) was used as the conductive agent and PTFE (F-106, DAIKIN Industries) as the binder. The Si/C composite, carbon black, and PTFE were premixed at a 96:1:3 weight ratio using a planetary mixer (ARE-310, THINKY) to ensure uniform dispersion of the components. The resulting mixture was manually kneaded with a mortar and pestle under shear force until a cohesive sheet formed. This sheet was rolled to a target thickness of ~85 μm using a roll-to-roll calendar to produce freestanding electrode sheets. These sheets were laminated onto SBR-pretreated copper current collectors to fabricate ThA. By contrast, PrL-ThA was laminated onto a Li/Cu foil (6.5 μm Li laminated on a 10 μm Cu substrate, MTI Korea, BR0182). The electrode density was controlled at 2.1 g cm^{-3} for both configurations, with an electrode area of 1.13 cm^2.

Cell assembly

Coin-type (CR2032, Wellcos Corporation) cells were assembled in a dry room with a dew point below −80 °C using a 19 mm polyethylene separator. For half-cell measurements, the electrolyte (Enchem) consisted of 1.15 M $LiPF_6$ in a 2:4:4 (by volume) mixture of ethylene carbonate, ethyl methyl carbonate, and diethyl carbonate, supplemented with 1 wt% vinylene carbonate and 10 wt% fluoroethylene carbonate (FEC). Lithium metal foil (thickness 1.0 T) was used as the counter electrode to assess the electrochemical performance of each dry-processed anode. For full-cell tests, Si/G anodes were paired with NCM811 and LFP. NCM811 cathodes were prepared with a weight ratio of NCM811: carbon black: binder = 90:5:5, while LFP cathodes were prepared with a weight ratio of LFP: carbon black: binder = 94.5:2.5:3. The full-cell electrolyte was identical to that used in the half cells, with an additional 1 wt% lithium difluorophosphate ($LiPO_2F_2$) for enhanced stability. All full cells were assembled with an N/P capacity ratio of 1.1 (capacity-based ratio), with the anodes punched to 14 mm in diameter and the cathodes to 12 mm.

Electrochemical measurement

The electrochemical performance of coin-type half cells was evaluated using galvanostatic charge–discharge cycling on a battery cycler (MIHW-200-160CH-B, NEWARE) under a constant current–constant voltage protocol. The cells were first subjected to two formation cycles at 0.1 and 0.2 C, followed by cycling at 0.3 C within a voltage range of 0.01–1.5 V (vs. Li/Li^+). CV was conducted at a scan rate of 0.1 mV s^{-1} in the same voltage window using a potentiostat (VSP, Biologic). EIS was performed using the same instrument over a frequency range of 250 kHz to 10 mHz with an amplitude of 5 mV (VSP, Biologic, Seyssinet-Pariset). For full-cell testing, Si/G anodes paired with NCM811 cathodes were cycled after two formation steps at 0.05 and 0.1 C, followed by evaluation at 0.2 C within a voltage range of 2.8–4.25 V. Full cells using LFP cathodes were cycled in a voltage window of 2.5–4.0 V under the same formation and cycling conditions. The raw impedance spectra obtained during charging were subsequently analyzed using a DRT framework. DRT analysis was performed with a MATLAB toolbox, which mathematically transforms the frequency-dependent impedance data into relaxation-time distributions, enabling the deconvolution and assignment of individual electrochemical processes. All electrochemical measurements were conducted at room temperature.

Characterization

The cross-section of the three-layer electrode was examined using a field-emission scanning electron microscope (FE-SEM; SU8220, Hitachi). Adhesion strength between the electrode and current collector was evaluated using a universal testing machine (Autograph AGS-X, SHIMADZU). XRD (D8 ADVANCE, Bruker) measurements were performed over a 2θ range of 10°–90° with a total scan time of 50 min. The NCM811 sample was prepared using a focused ion beam (SCIOS, FEI) to obtain electron-transparent cross-sectional lamellae. High-resolution structural analysis was further conducted using aberration-corrected TEM. TOF-SIMS (TOF-SIMS 5, ION TOF) data were collected using a pulsed Bi^{3+} ion at 25 keV, and in-depth XPS (K-alpha, ThermoFisher) was performed with a 2 keV Al Kα X-ray source.

Computational method

Molecular Dynamics simulations were used to investigate interfacial interactions between the PTFE binder and anode components using BIOVIA Materials Studio 2025 (Accelrys Inc.). Composite structures were generated through packing calculations, followed by geometry optimization using the Condensed-phase Optimized Molecular Potentials for Atomistic Simulation Studies force field with fine convergence tolerance[1]. All structures underwent a 50 ps pre-cell relaxation stage under the NPT (isothermal–isobaric) ensemble. Temperature and pressure were maintained at room conditions (25 °C and 1 bar) using the Nose–Hoover–Langevin thermostat and Berendsen barostat, respectively. Simulation employed a time step of 1 fs and cut-off radius of 1.85 nm for Van der Waals interactions. Long-range electrostatic interactions were calculated using the Ewald summation method[2]. PTFE and SBR chains were constructed with five monomer repeat units each[3]. Atomic charges were derived from density functional theory calculations using the DMol3 module. Convergence tolerance was set at 0.002 Ha $Å^{-1}$ for maximum force, 1.0×10^{-5} Ha for energy, and $< 1.0 \times 10^{-6}$ Ha for self-consistent field tolerance, using a numerical basis set based on double numerical plus polarization. The lithium adhesion energy was calculated using the following equation: $E_{adhesion\ energy} = E_{total} - E_{substrate} - E_{adsorbate}$. Here, $E_{substrate}$ and $E_{adsorbate}$ denote the energy of PTFE and the adsorbate, SBR or Li metal, respectively.

FEM-based theoretical analysis

Finite element analysis was performed to investigate the prelithiation behavior of SiC composite electrodes under both direct contact and electrochemical conditions. Simulations were performed using the Doyle–Fuller–Newman (DFN) model within COMSOL Multiphysics (version 6.2). A 3D microstructure representing the SiC composite electrode was constructed by sequentially stacking silicon and carbon particles within a 50 μm thick domain. Geometric generation was conducted using Blender 4.3, a commercial 3D modeling software, and imported into COSMOL as the computational mesh[4,5].

The current density vector i_s, which describes the flow of electrons through the cross-sectional area of the solid electrode, is proportional to the gradient of the electric potential $\nabla\phi_s$, and is characterized by Ohm's law:

$$i_s = -\sigma_s \nabla\phi_s, \#(1)$$

where σ_s and ϕ_s represent the intrinsic electrical conductivity of the electrode material and the electric potential at the solid electrode region, respectively. The transport behavior of the charged lithium species in the liquid electrolyte was calculated based on a modified form of Ohm's law, which accounts for both electric potential and concentration gradients, as follows:

$$i_l = -\sigma_l \nabla\phi_l + \frac{2\sigma_l RT}{F}\left(1 + \frac{\partial lnf}{\partial lnc_l}\right)(1 - t_+)\nabla lnc_l, \#(2)$$

where σ_l, ϕ_l, F, R, f, c_l, and t_+ represent the ionic conductivity of liquid electrolyte, potential at the liquid electrolyte region, Faraday constant, universal gas constant, molar activity coefficient, concentration of liquid electrolyte, and transport number of the liquid electrolyte, respectively. The time-dependent Li-ion mass transportation, which accounts for both concentration-driven diffusion and migration under the influence of ionic current in liquid electrolyte, is described by Fick's second law of diffusion:

$$\frac{\partial c_l}{\partial t} = \nabla \cdot \left(D_l \nabla c_l\right) - \frac{i_l t_+}{F},\#(3)$$

where D_l represents the diffusion coefficient of Li ions in the liquid electrolyte region.

The time-dependent Li-ion mass transportation, both across adjacent active material particles via direct contact and within individual particles, is described by Fick's second law of diffusion, as follows:

$$\frac{\partial c_s}{\partial t} = \nabla \cdot \left(D_s\left(\nabla c_s\right)\right),$$

(4)

where D_s and c_s represent the diffusion coefficient and concentration of Li-ion in the active material, respectively[6,7]. Local current density i, representing the interfacial electrochemical kinetics driven by the potential difference between the electrolyte and the active material, was calculated using the generalized Butler–Volmer equation, as follows:

$$i = i_0\left(\exp\left(\frac{(1-\alpha)F\eta}{RT}\right) - exp\left(\frac{\alpha F\eta}{RT}\right)\right),\#(5)$$

where α, η, and i_0 represent cathodic charge exchange coefficient of active materials, overpotential, and exchange current density[8].

Supplementary Note 1

The prelithiation amount was carefully designed to match the first-cycle irreversible lithium loss of the anode. Excessive prelithiation beyond this compensation can cause undesired lithium metal plating, dead lithium formation, or unstable SEI growth, thereby compromising the long-term cycling stability and safety of the cell.[1,2] Accordingly, the measured first-cycle irreversible capacity loss of the anode was 68.9 mAh g^{-1} with an areal mass loading of 13.7 mg cm^{-2}, corresponding to an areal capacity of 0.943 mAh cm^{-2}. Based on this value, the lithium thickness was selected as 6.5 μm, corresponding to 1.34 mAh cm^{-2} areal capacity, calculated using the following equation:

$$Q_{Li} = \rho_{Li} \times h \times C_{th},$$

where ρ_{Li} (= 0.534 g cm^{-3}) is the density of lithium, C_{th} (= 3860 mAh g^{-1}) is the theoretical capacity of lithium, and h is the lithium thickness (cm).[3,4] This amount was sufficient to fully compensate the irreversible capacity loss while minimizing the risks associated with excessive prelithiation.

Supplementary Note 2

The energy density in a full cell is calculated as follows:

$$\begin{aligned} &Energy\ Density\ at\ the\ Electrode\ Level\ \left(Wh\ Kg^{-1}\right) \\ &\quad = Gravimetric\ Capacity\ \times Nominal\ Voltage\ \times Active\ Material\ Ratio \\ &\quad \times \frac{Mass\ Lading\ (cathode)}{Mass\ Loading\ (Cathode\ + Anode)}. \end{aligned}$$

The detailed electrode information for both the cathode and anode is provided in Table S2.

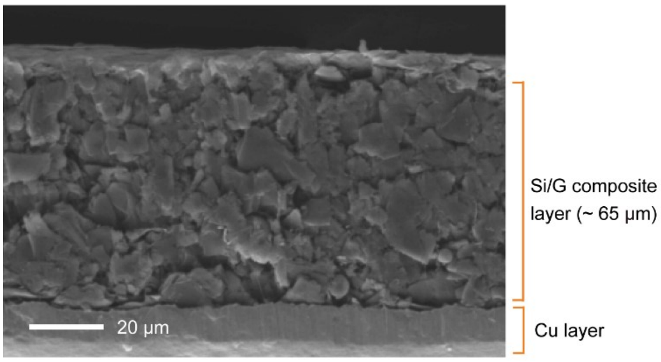

Fig. S1 Cross-sectional SEM image of the ThA.

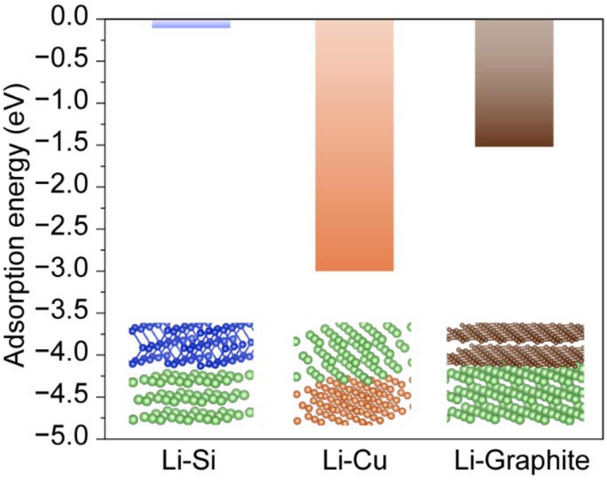

Fig. S2 Calculated adsorption energies of materials consisting of an electrode composite layer and substrate for Li.

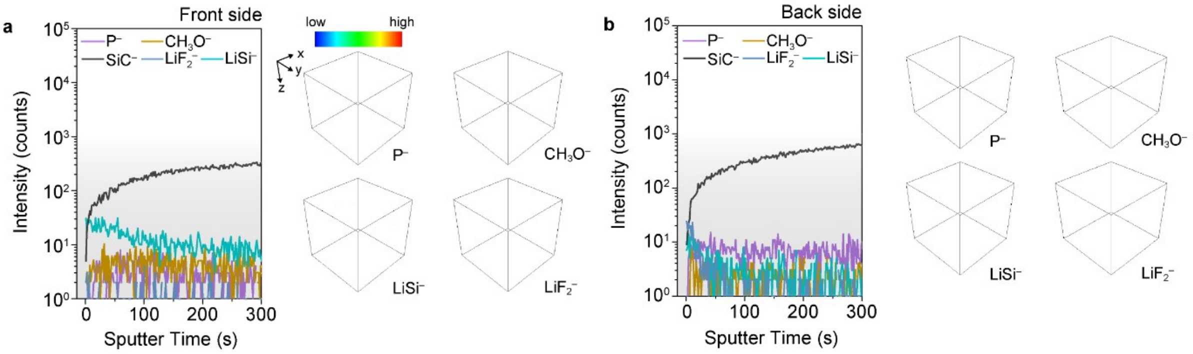

Fig. S3 TOF-SIMS profiles of **a**, front and **b**, back of pristine ThA and corresponding 3D reconstruction images without electrolyte exposure.

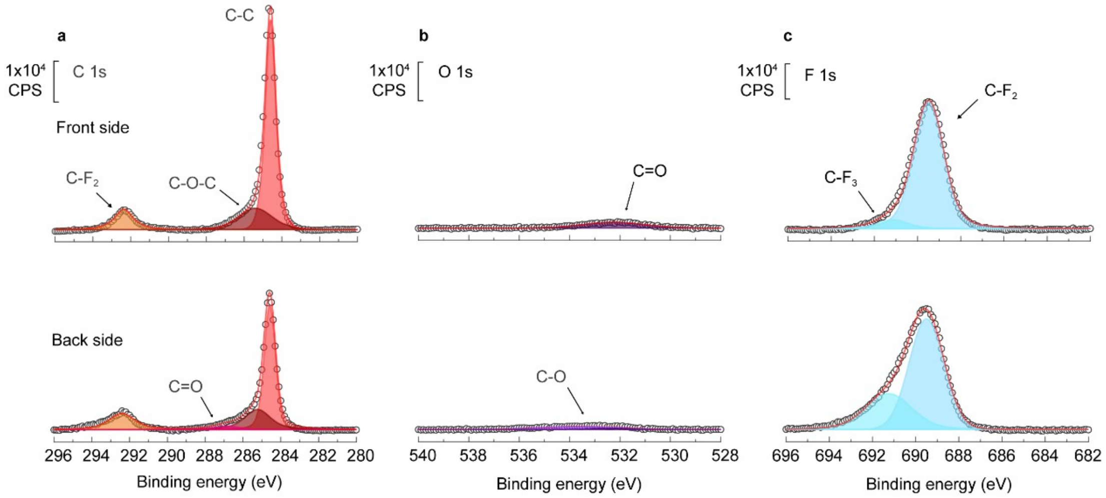

Fig. S4 a, C 1s, **b,** O 1s, and **c,** F 1s XPS profiles of the front and back surfaces of the pristine ThA.

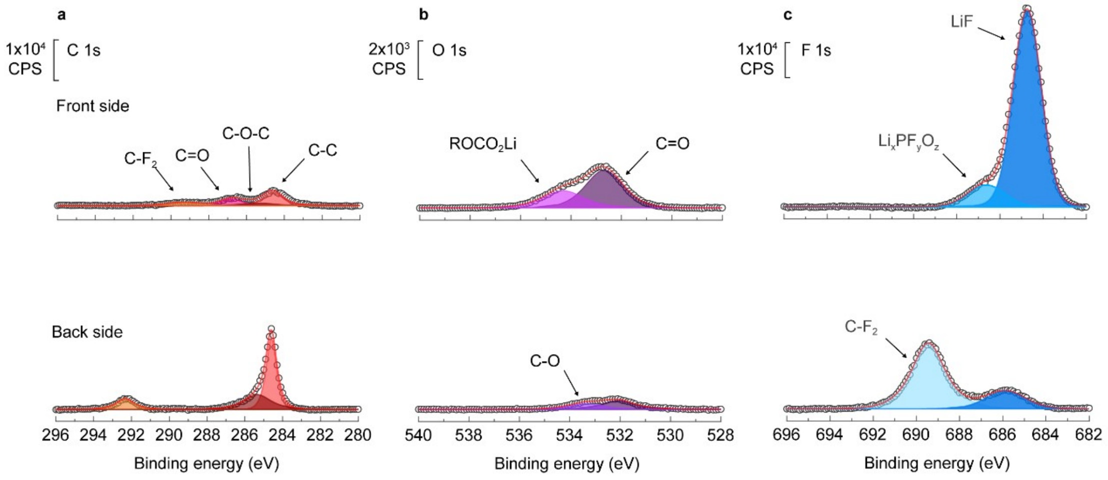

Fig. S5 **a,** C 1s, **b,** O 1s, and **c,** F 1s XPS profiles of the front and back surfaces of ThA immersed for 24 h.

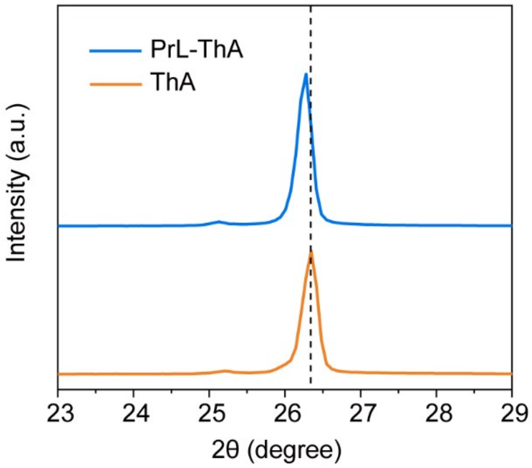

Fig. S6 XRD patterns of pristine electrodes without contact with electrolytes.

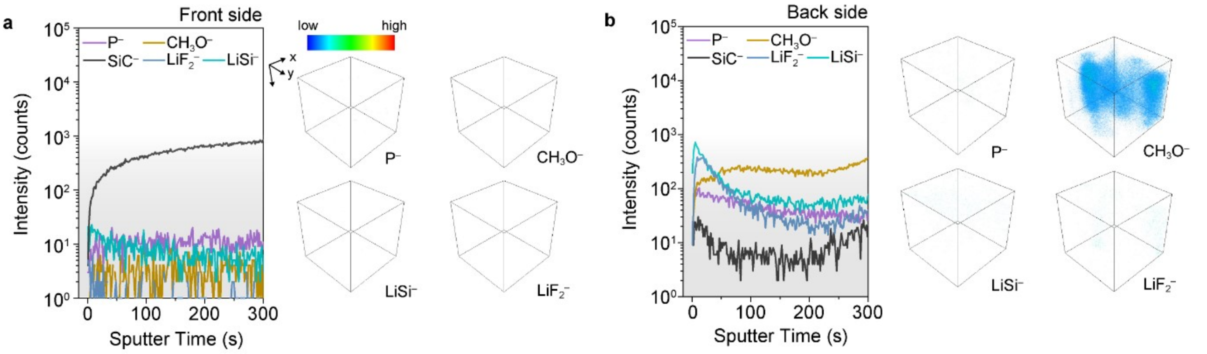

Fig. S7 TOF-SIMS profiles of **a**, front and **b**, back of pristine PrL-ThA and corresponding 3D reconstruction images.

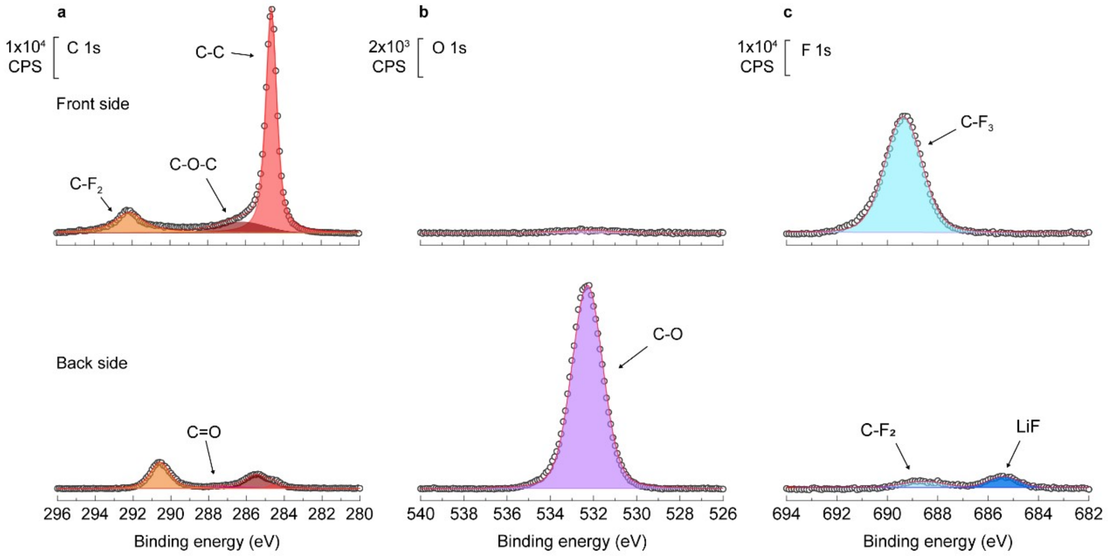

Fig. S8 a, C 1s, **b,** O 1s, and **c,** F 1s XPS profiles of the front and back surfaces of pristine PrL-ThA.

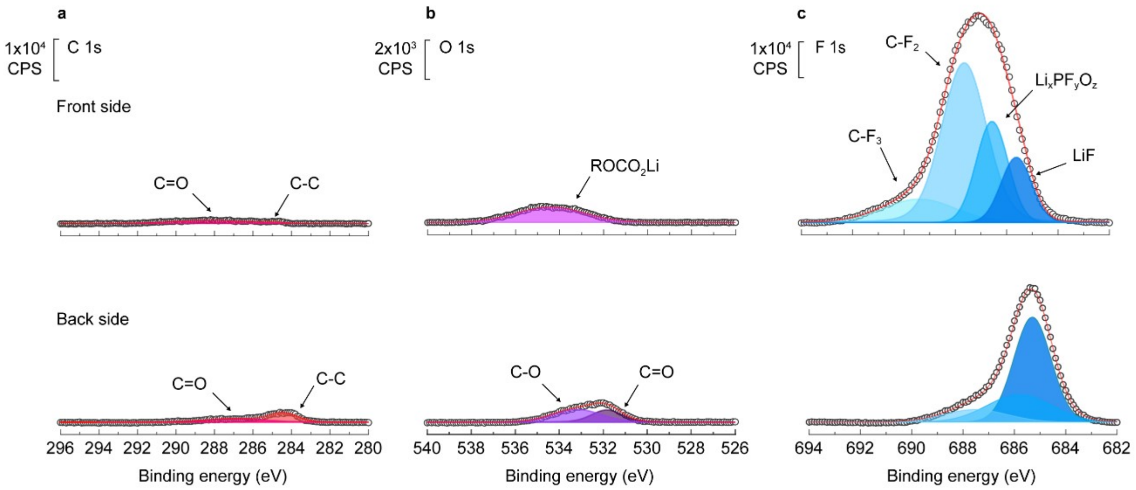

Fig. S9 a, C 1s, **b,** O 1s, and **c,** F 1s XPS profiles of the front and back surfaces of PrL–ThA-immersed for 24 h.

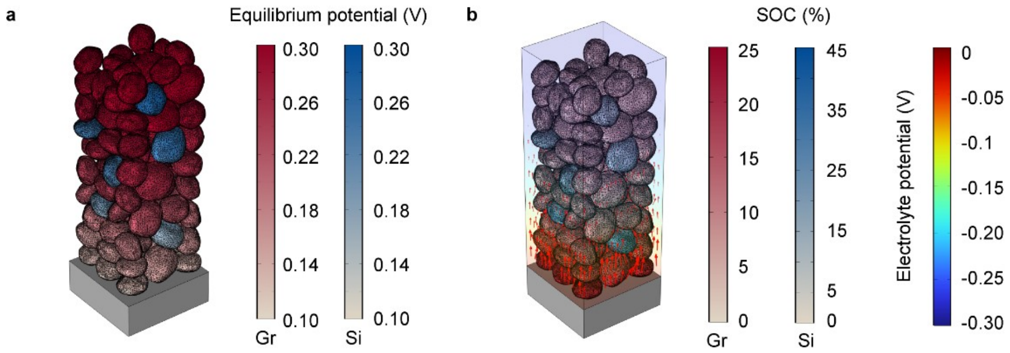

Fig. S10 PrL-ThA electrode under liquid electrolyte conditions. **a,** overpotential distribution and **b,** electrolyte potential distribution with SOC of the active materials.

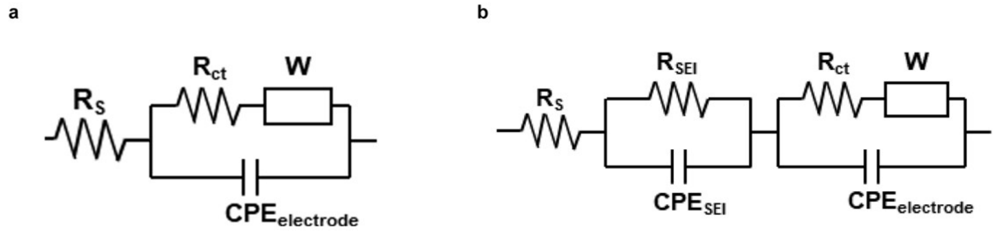

Fig. S11 Equivalent circuits of EIS measurement of **a,** before and **b,** after formation shown in Fig. 4c and d, respectively.

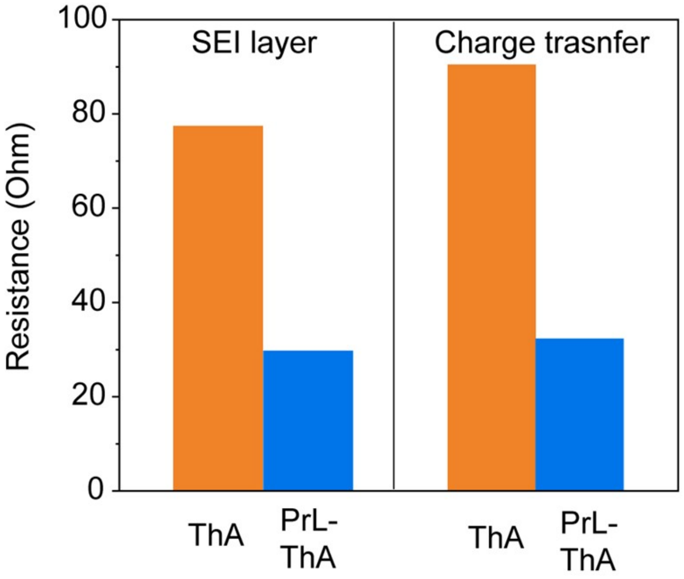

Fig. S12 Comparison of R_{SEI} and R_{ct} after formation of ThA and PrL-ThA. PrL-ThA results in lower R_{SEI} and R_{ct} values compared with that of the untreated ThA after formation.

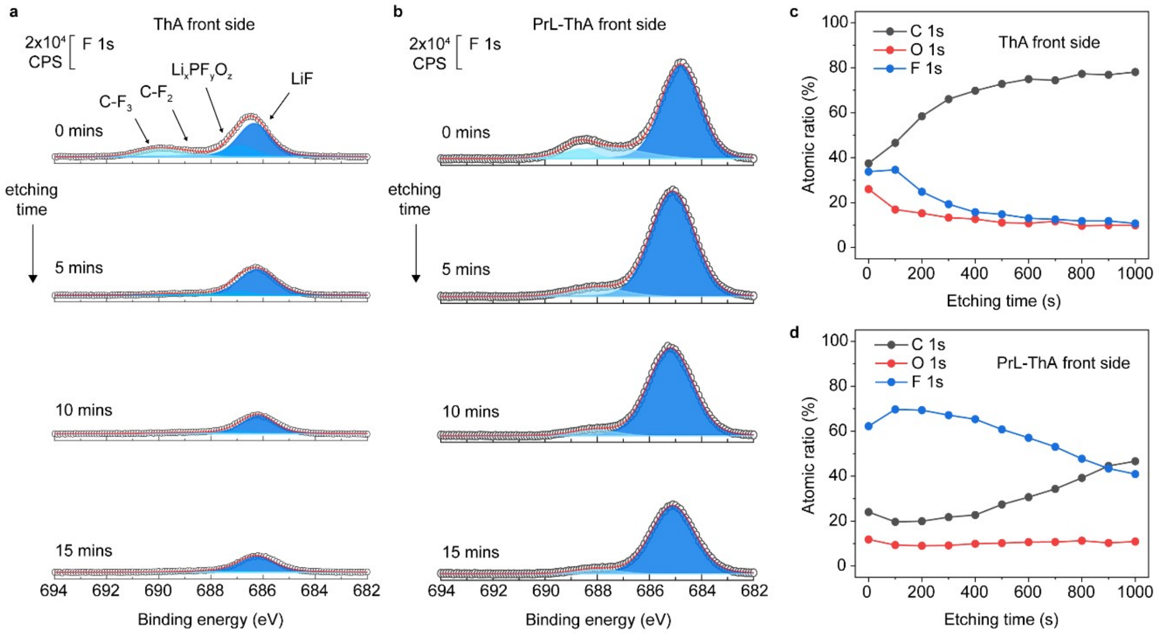

Fig. S13 XPS analysis results of the electrodes after formation. In-depth F 1s XPS spectra and atomic ratio profiles of the front of **a, c,** ThA and **b, d,** PrL-ThA.

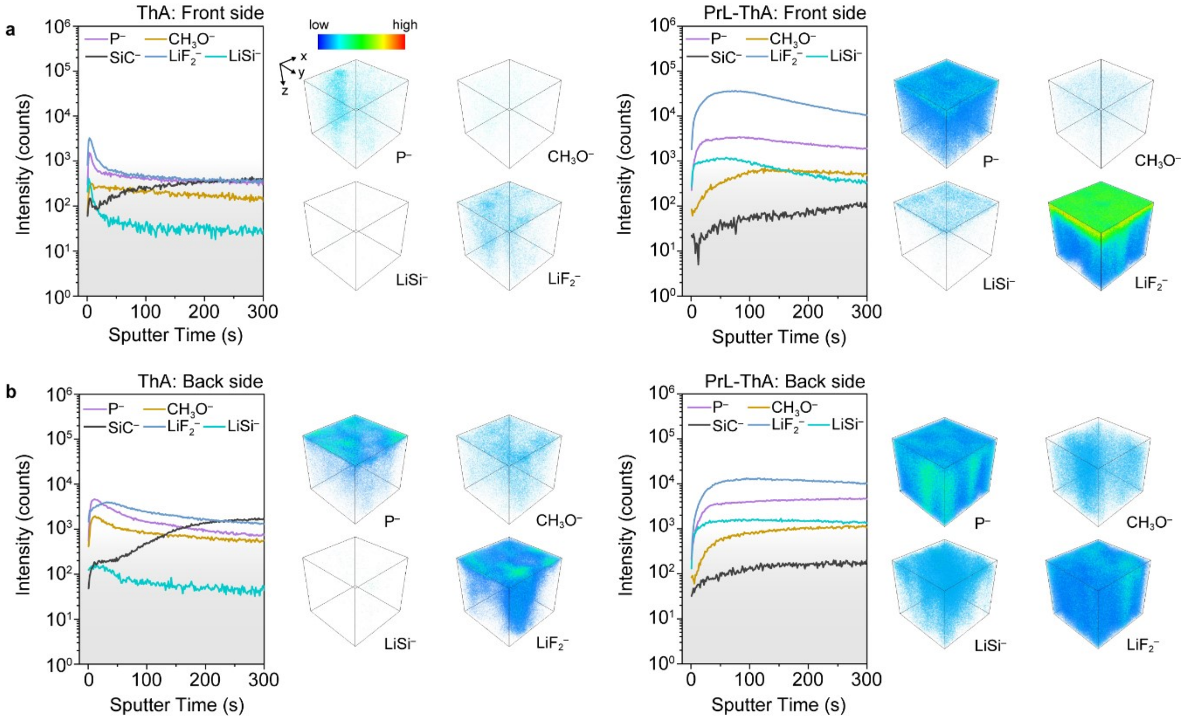

Fig. S14 TOF-SIMS profiles of **a**, front and **b**, back of the electrodes after the formation of ThA (left) and PrL-ThA (right) and corresponding 3D reconstruction images.

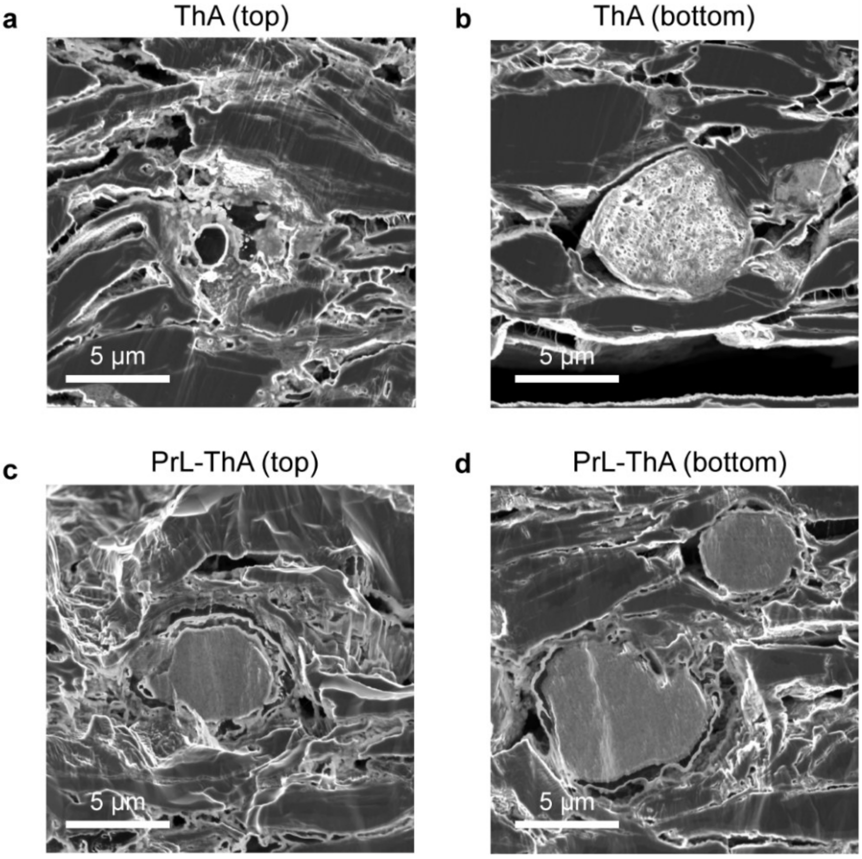

Fig. S15 Cross-sectional images of Si particles in anodes after 20 cycles at 0.3 C in a half-cell configuration. The **a,** top and **b,** bottom of ThA, and **c,** top and **d,** bottom of PrL-ThA.

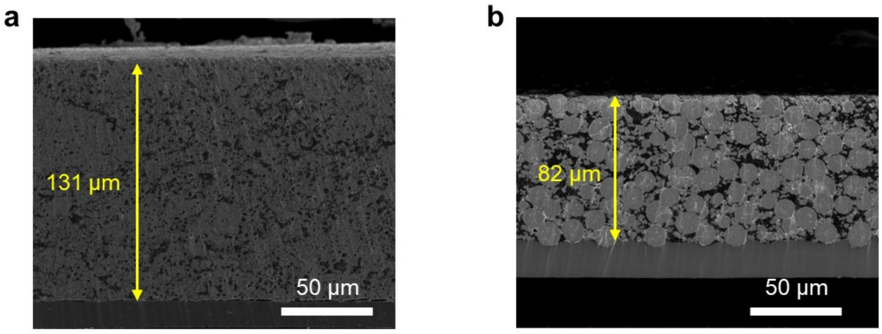

Fig. S16 Cross-sectional SEM images of **a,** LFP and **b,** NCM811 electrodes, with thicknesses of 131 μm and 82 μm, respectively.

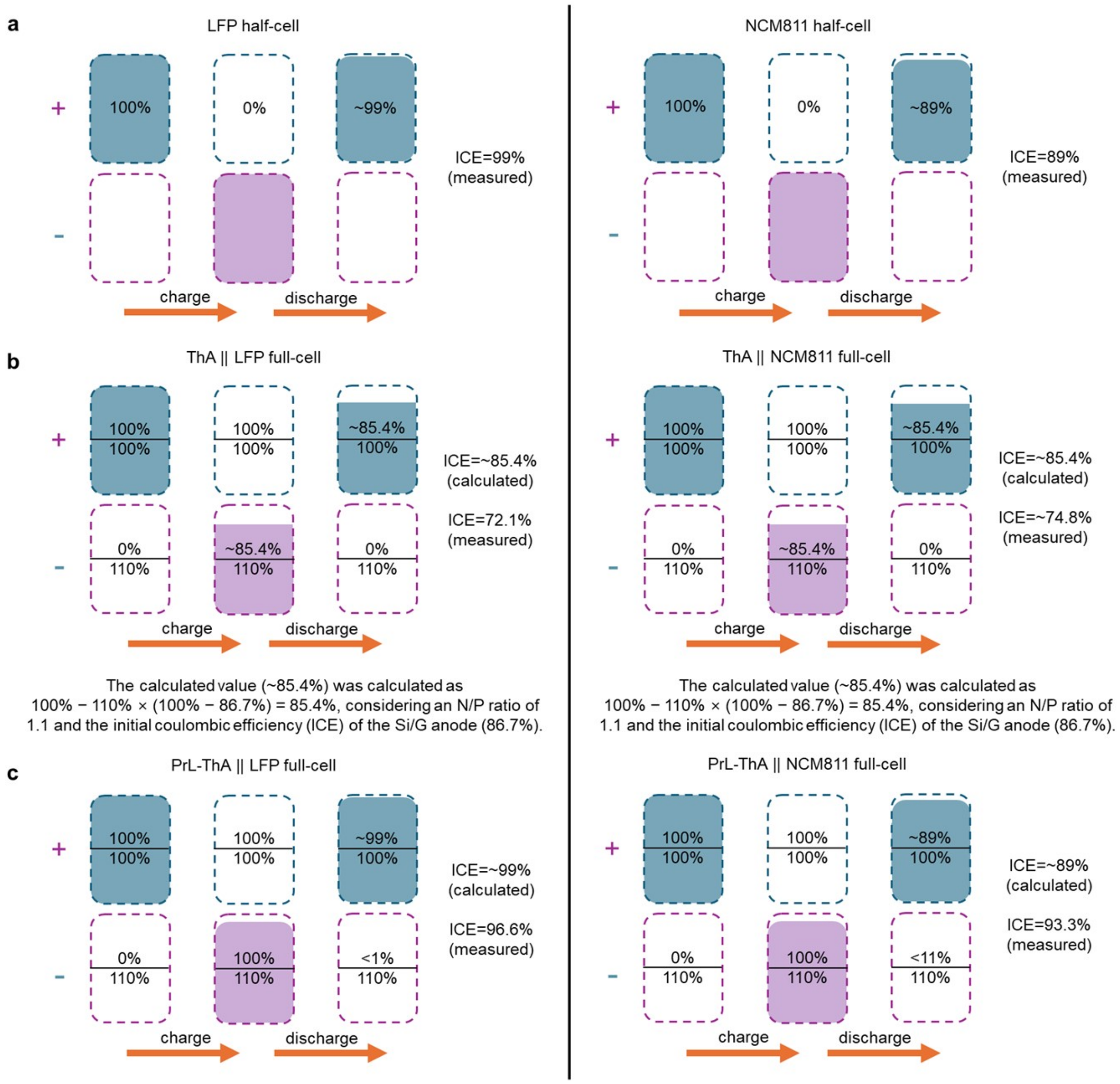

The calculated value (~85.4%) was calculated as 100% − 110% × (100% − 86.7%) = 85.4%, considering an N/P ratio of 1.1 and the initial coulombic efficiency (ICE) of the Si/G anode (86.7%).

The calculated value (~85.4%) was calculated as 100% − 110% × (100% − 86.7%) = 85.4%, considering an N/P ratio of 1.1 and the initial coulombic efficiency (ICE) of the Si/G anode (86.7%).

Fig. S17 Schematic illustration of Li source inventory changes in (a) LFP and NCM811 half-cell, and LFP and NCM811 full-cell with (b) ThA and (c) PrL-ThA at initial formation cycle. Calculated ICE on (b) is based on the ideal condition, where no irreversible capacity loss occurs at the cathode, and therefore, the measured ICE is lower than calculated ICE.

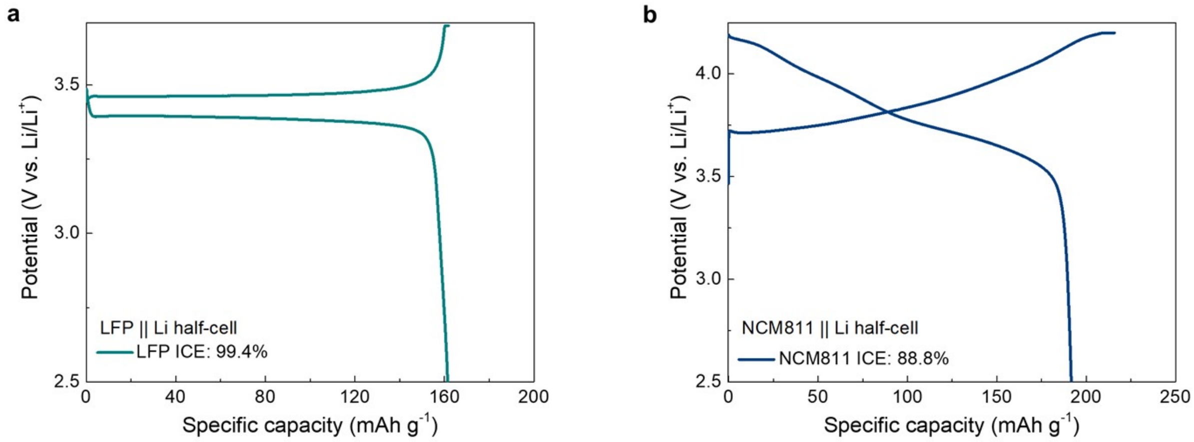

Fig. S18 Voltage profiles of each cathode in a half-cell configuration. The measurements were conducted within their respective voltage windows, with **a,** LFP (2.5–3.7 V) showing an ICE of 99.4% and **b,** NCM811 (2.5–4.2 V) showing an ICE of 88.8%.

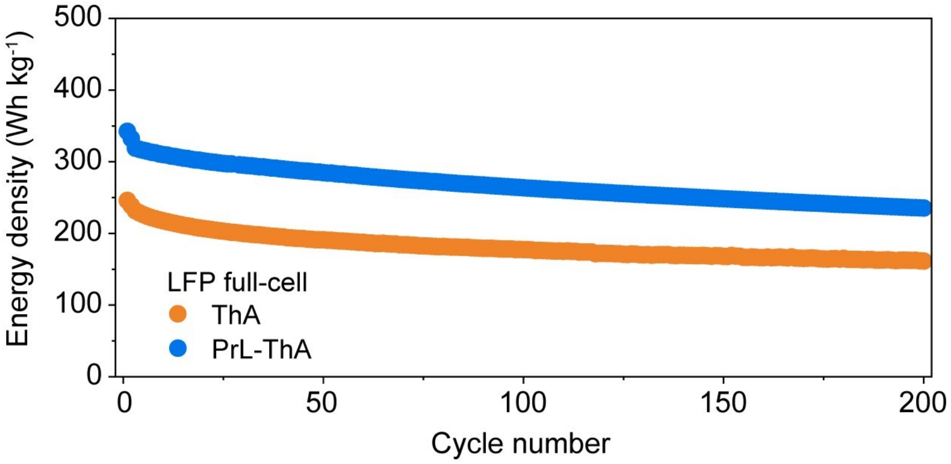

Fig. S19 Energy densities of ThA||LFP and PrL-ThA||LFP full cells during extended cycling, demonstrating the stable performance of PrL-ThA over 200 cycles.

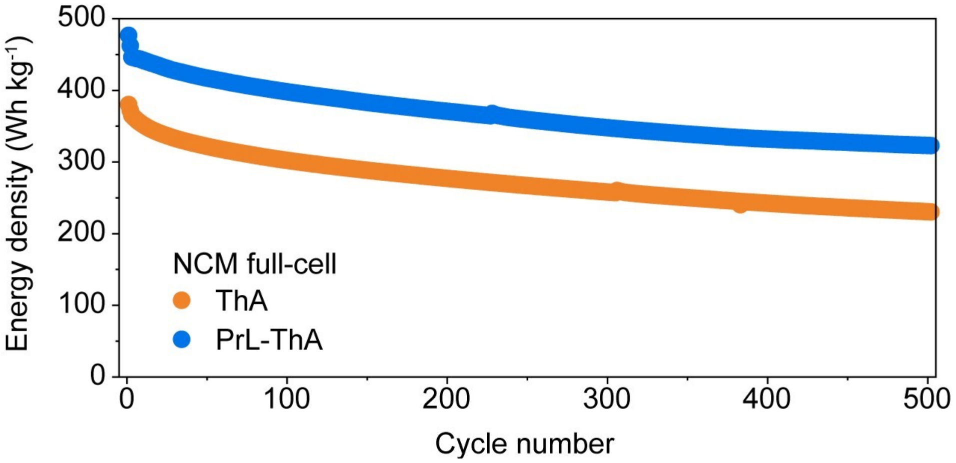

Fig. S20 Energy densities of ThA||LFP and PrL-ThA||LFP full cells during extended cycling, demonstrating the stable performance of PrL-ThA over 500 cycles.

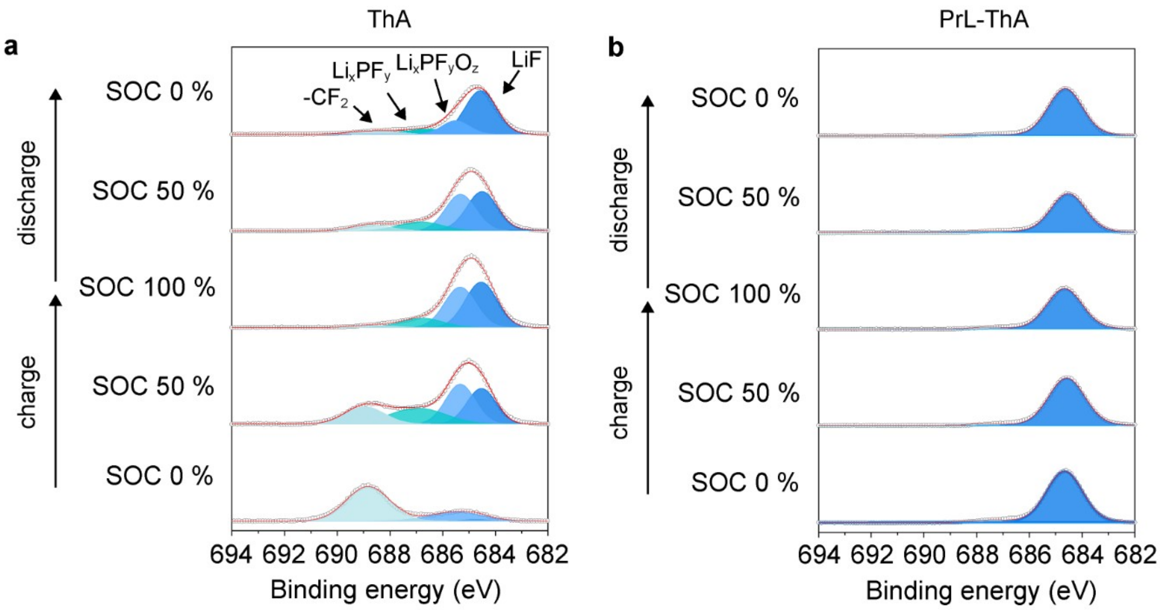

Fig. S21 F 1s XPS profiles of (a) ThA and (b) PrL-ThA back side by state of charge during the initial formation cycle in the NCM811 full-cell configuration.

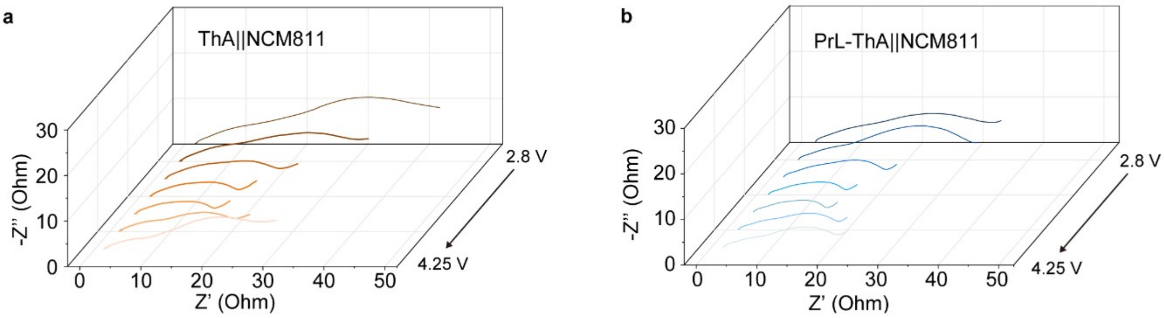

Fig. S22 EIS raw data of in-situ DRT spectra of NCM811 full-cells with (a) ThA and (b) PrL-ThA during the first formation charge from 2.8 to 4.25 V.

Table S1. EIS fitting results for ThA and PrL-ThA before and after the formation cycle.

Samples	Before formation			After formation			
	R_s (ohm)	R_{ct} (ohm)	R_{total} (ohm)	R_s (ohm)	R_{SEI} (ohm)	R_{ct} (ohm)	R_{total} (ohm)
ThA	1.5	344.8	346.3	2.2	77.3	90.5	202.1
PrL-ThA	1.5	207.6	209.1	1.6	27.8	30.8	60.2

Table S2. Detailed description of electrode properties and cell design.

System	LFP full-cell				NCM811 full-cell			
	ThA		PrL-ThA		ThA		PrL-ThA	
Electrode	Anode	Cathode	Anode	Cathode	Anode	Cathode	Anode	Cathode
Active Loading level (mg cm^{-2})	13.13	30.59	12.94	30.84	13.11	26.3	13.13	26.32
Loading level (mg cm^{-2})	13.57	32.37	13.47	32.63	13.65	29.22	13.57	29.24
Thickness (μm)	65	131	63	131	65	82	63	82
Specific capacity (mAh g^{-1})	428.27	163	428.27	163	428.27	191.82	428.27	191.82
N/P ratio	1.1	1.1	1.1	1.1	1.1	1.1	1.1	1.1

Table S3. Summary of reported prelithiation approaches, full-cell architectures, and corresponding electrochemical performances, including those without prelithiation for comparison.

Ref.	**Anode**	**Cathode**	**Pre-lithiation strategy**	**Initial CE (%)**	**Cathode Loading Level (mg cm^{-2})**	**Anode Loading Level (mg cm^{-2})**	**Cycle number**	**Areal capacity (mAh cm^{-2})**
This work	Si/G	NCM811	Roll-to-Roll	93.3	26.3	13.13	500	5.63
S9	Si/C composite	NCM111	Transfer-printing	89.21	6	4.5	100	2.03
S10	Si	NCM523	Li foil	84.7	10	1	300	2.47
S11	Si@SiO_2	NCM811	Li-metal contact	84	11.5	2.5	200	2.5
S12	GNP-Si/G	NCM622	None	85.7	17.88	7.15	300	3.6
S13	μ-Si	NCM811	Li thermal evaporation	77	4.28	1.02	150	3.08
S14	SiO_x/G/C	NCM	Li foil	73	N/A	1.2	100	0.24
S15	μ-Si (CFD)	NCM811	Electrochemical	85.4	9.3	0.65	500	2.2
S16	Si-G	NCM811	None	82.7	14.6	5.75	100	3.0

Supplementary References

1 R. L. C. Akkermans, N. A. Spenley and S. H. Robertson, *Mol. Simul.*, 2021, 47, 540–551.

2 S. Lee, H. Lee, H. Chang, M. Lim, M. Lee, B. Koo, K.-E. Ryou, S.-M. Bak, H. Lee, S. Chae, J. Moon and H. Lee, *ACS Nano*, 2025, 19, 15789–15802.

3 P. Li, Y. Hou, H. Chen, Y. Bai, D. Yang, Q. Sheng, S. Zhu and L. Yu, *Mater. Today Commun.*, 2024, 40, 109892.

4 J. Moon, T. D. Hoang, S. Soo Park, S. Park, D. Y. Rhee, J. Lee, S. A. Han, M.-S. Park and J. H. Kim, *J. Ener. Chem.*, 2022, 71, 470–477.

5 H. Lee and D. Kim, *Multiscale Science and Engineering*, 2023, 5, 119–125.

6 D. W. Kang, S. S. Park, H. J. Choi, J.-H. Park, J. H. Lee, S.-M. Lee, J.-H. Choi, J. Moon and B. G. Kim, *ACS Nano*, 2022, 16, 11892–11901.

7 J. Y. Kim, S. Jung, S. H. Kang, J. Park, M. J. Lee, D. Jin, D. O. Shin, Y. Lee and Y. M. Lee, *Adv. Energy Mater.*, 2021, 12, 2103108.

8 H. Jo, J.-W. Lee, E. Kwon, S. Yu, B. G. Kim, S. Park, J. Moon, M. J. Ko and H.-D. Lim, *ACS Nano*, 2024, 18, 35718–35728.

9 C. Yang, H. Ma, R. Yuan, K. Wang, K. Liu, Y. Long, F. Xu, L. Li, H. Zhang, Y. Zhang, X. Li, H. Wu, *Nat, Energy,* 2023 8, 703–713.

10 Y. Li, L. Lv, R. Liang, L. Wang, Y. Wang, Q. Qu, M. Shen, H. Zheng, *J. Mater. Chem. A,* 2024, 12, 20045–20055.

11 Y. Zhang, R. Zhang, S. Chen, H. Gao, M. Li, X. Song. H. L. Xin, Z. Chen, *Adv. Funct. Mater.,* 2020, 30, 2005956.

12 S. Park. M. Choi, J. Lee, S. Lee, J. Kim, T. Yun. N. Kim, J. Sung, J. Cho, M. Ko, S. Chae, *Small,* 2025, 21, 2404949.

13 E. Adhitama, M. M. Bela, F. Demelash, M. C. Stan, M. Winter, A. Gomez-Matrin and T. Placke, *Adv. Ener. Mater.*, 2023, 13, 2203256.

14 K. Zhang, J. Xing, H. Peng, J. Gao, S. Ai, Q. Zhou, D. Yang, X. Gu, *Energy Mater.* 2024, 4, 400043.

15 T. Lee, M. J. Seong, H. C. Ahn, M. Baek, K. Park, J. Oh, T. Choi, J. W. Choi, *Proc. Nat. Acad. Sci.* 2025, 122, e2417053121.

16 D. Lee, W. Jeong, J. Lee, H. E. Yoo, S. Sun, C. Lee, J. Kim, Y. Kim, M. Yoon, P. J. Kim, U. Paik, J. W. Lee, T. Song, J. Choi, *Int. J. Ener. Res.* 2025, 1198001.